Acta Mech
https://doi.org/10.1007/s00707-026-04664-y

ORIGINAL PAPER

Rajendran Selvamani · Thangamuni Prabhakaran · Murat Yaylacı · Dursun Murat Sekban · Ecren Uzun Yaylacı

Dynamic behavior of graphene-origami-based meta-auxetic doublet nanobeam with memory-dependent effect

Received: 22 December 2025 / Revised: 9 February 2026 / Accepted: 15 February 2026
© The Author(s) 2026

Abstract This work explores the mechanical characteristics response electro-magneto-thermoelastic (EMT) nanobeams by simultaneously accounting for fractional viscoelasticity, nonlocal elastic interactions, doublet mechanics, and couple-stress effects. A meta-auxetic architecture is integrated into the nanobeam inspired by graphene-based origami structures, allowing its mechanical behavior to be tuned through geometric reconfiguration and engineered microstructural features. Time-dependent viscoelastic phenomena—such as nanoscale stress relaxation and strain evolution—are captured using the Caputo-form Atangana–Baleanu fractional operator representing the material's memory characteristics. The governing relations are formulated through Hamilton's principle under a nonlocal couple-stress formulation. Because these equations are nonlinear and fractional in nature, the Adomian decomposition technique (ADT) is applied to obtain analytical solution approximations. A comparative study with previously published results is carried out for model verification. The results demonstrate that couple-stress behavior, fractional-order memory effects, auxetic properties arising from graphene-origami structures, doublet mechanics, and nonlocal phenomena all strongly influence the stress–strain behavior and thermal response of the nanobeam. Overall, the study offers important guidelines for designing and optimizing next-generation nanoscale systems, including biomedical sensors, reconfigurable electronics, adaptive façade components, and intelligent infrastructural materials.

1 Introduction

The rapid evolution of nanotechnology has been strongly driven by advances in graphene synthesis and processing. Early breakthroughs included the fabrication of large-area ultrathin films from reduced graphene oxide

R. Selvamani · T. Prabhakaran
Department of Mathematics, Karunya Institute of Technology and Sciences, Karunya Nagar, Coimbatore, Tamilnadu 641114, India

M. Yaylacı (✉)
Department of Civil Engineering, Recep Tayyip Erdogan University, 53100 Rize, Türkiye
e-mail: murat.yaylaci@erdogan.edu.tr

M. Yaylacı
Turgut Kıran Maritime Faculty, Recep Tayyip Erdogan University, 53900 Rize, Türkiye

M. Yaylacı
Dijitalpark Teknokent Murat Yaylacı-Luzeri R&D Engineering Company, 53100 Rize, Türkiye

D. M. Sekban
Department of Marine Engineering Operations, Karadeniz Technical University, Trabzon 61080, Türkiye

D. M. Sekban
Trabzon Teknokent, WMS Engineering Services Industry Trade Limited Company, Trabzon 61080, Türkiye

E. Uzun Yaylacı
Faculty of Fisheries, Recep Tayyip Erdogan University, 53100 Rize, Türkiye

Published online: 30 March 2026

[1] and the development of stable water-based dispersions of graphene nanosheets [2], which enabled the realization of lightweight, flexible, and highly conductive materials. These advances facilitated a wide range of nanoelectromechanical applications, including micromechanical mass sensing [3], enhanced resonance-shift accuracy in microcantilevers [4], and graphene-based nonvolatile memory devices [5]. Owing to its exceptional mechanical strength, ultralow mass density, and superior electromechanical performance, graphene has emerged as a key material platform for next-generation nanoelectromechanical systems (NEMS). Beyond material synthesis, recent research has increasingly focused on architected graphene-based nanostructures, where geometry is intentionally engineered to achieve unconventional mechanical responses. In this context, origami- and kirigami-inspired designs have attracted significant attention as effective strategies for tailoring mechanical behavior through folding, cutting, and controlled out-of-plane deformation. When applied to graphene, origami architectures exploit its atomic-scale thickness and high flexibility, allowing large reversible deformations without material failure. By carefully designing fold patterns and hinge-like geometries, graphene-origami structures can exhibit auxetic behavior, characterized by a negative Poisson's ratio whereby the structure expands laterally when stretched axially. Since this behavior arises from geometric configuration rather than intrinsic material properties, such systems are classified as meta-auxetic materials. Recent studies have demonstrated that auxetic responses can be realized in graphene-derived structures through patterned cuts, fold-guided buckling, and reconfigurable hinge mechanisms. These geometrically induced transformations enable significant tunability of effective stiffness, deformation modes, and wave propagation characteristics, making graphene-origami-based meta-auxetic nanostructures a promising platform for programmable and multifunctional mechanical behavior at the nanoscale. From a fabrication standpoint, graphene-origami and kirigami architectures are increasingly feasible due to advances in nanoscale patterning and strain-engineering techniques. Experimental approaches such as electron-beam and photolithographic patterning followed by substrate-induced self-folding, focused ion beam or laser-assisted cutting, chemical functionalization-driven folding, and van der Waals-assisted stacking have been reported for producing folded and reconfigurable graphene nanostructures. The combination of auxetic behavior, ultralow mass density, and high stiffness makes graphene-origami-based nanobeams particularly attractive for advanced NEMS applications. Potential applications include ultrasensitive resonant mass sensors, tunable nanoresonators, adaptive vibration control elements, flexible and stretchable electromechanical devices, and reconfigurable waveguides. Moreover, accurately capturing time-dependent and history-dependent material behavior is essential for modeling nanostructures operating under dynamic loading conditions, where viscoelasticity, internal friction, and long-range interactions play a critical role. At the structural level, extensive mechanical modeling of nanomaterials has been developed to describe size-dependent and microstructural effects. Early investigations addressed the stability of conveying carbon nanotube systems under magnetic fields [6], internal resonances in MEMS arches [7], and combined experimental–analytical studies on multilayered microbeams [8]. Subsequent research examined thermoelastic behavior and vibration characteristics of nanobeams subjected to harmonic and thermal excitations [9]. A major theoretical advancement was introduced through Eringen's nonlocal elasticity theory [10, 11], which accounts for long-range interatomic interactions and has been widely applied to wave propagation in carbon nanotubes [12], functionally graded nanobeams [13–17], and magneto-thermoelastic nanostructures [18]. Further studies investigated nonlocal porous beams in fluid environments [19, 20] and thermoviscoelastic graphene sheets interacting with elastic substrates [21]. To capture microstructural interactions more accurately, doublet mechanics have been introduced as an effective modeling framework. This approach has been successfully applied to mass-sensing nanobeams [22], generalized nonlocal strain-gradient magneto-piezo-thermoelastic beams [23], piezo-magneto-thermoelastic functionally graded nanobeams in fluid media [24], and nonlinear poro-thermoelastic vibrations in layered shells [25]. Nonlinear forced vibration under moving loads was examined in [26], while the granular mechanics underlying doublet theory were discussed in foundational work on microstructural mechanics [27]. Subsequent bending analyses of Euler–Bernoulli and Timoshenko nanobeams using doublet mechanics were reported in [28]. In parallel, advanced analytical and semi-analytical solution techniques have been developed to address the strong nonlinearity of nanostructural governing equations. Adomian presented a comprehensive formulation of the Adomian decomposition method (ADM) for nonlinear differential equations [29], which was later applied to free vibration analysis of Euler–Bernoulli beams with high computational efficiency [30]. Combined nonlocal and surface energy effects on nanobeam vibrations were investigated in [31], followed by further studies on nonlocal beam bending, buckling, and vibration [32]. To model time-dependent material behavior, fractional derivative concepts were introduced to capture complex viscoelastic responses [33, 34], with improved formulations eliminating singular kernels [35, 36]. These developments enabled fractional thermoelastic models [37] and memory-dependent thermoelastic analyses of nanobeams subjected to periodic heat flux and laser pulse heating [38–40]. More recently,

attention has shifted toward metamaterial-inspired nanostructures, where geometry and material behavior are co-designed to achieve enhanced functionality. Graphene-origami-enabled magnetostrictive nanoplates exhibiting unique buckling characteristics were reported in [41], while origami-based auxetic metamaterial beams demonstrated rich nonlinear forced vibration responses in [42]. Tunable mechanical behavior based on Miura and herringbone core geometries was explored in [43], alongside bio-inspired helicoidal composite cylinders [44]. Reconfigurable hard-magnetic soft composites have also emerged as promising candidates for multifunctional and adaptive systems [45]. Further extensions of metamaterial-based nanobeam modeling have incorporated coupled nonlocal elasticity, fractional derivatives, surface energy, and couple-stress effects to investigate magnetoelastic wave propagation, vibration, and stability characteristics of advanced nanostructures [46–50]. Ghannadpour et al. [51] utilized the Ritz method to study bending, buckling, and vibration in nonlocal Euler beams, demonstrating the role of small-scale effects. Phadikar and Pradhan [52] formulated a variational approach and applied the finite element method (FEM) to model nanobeams and nanoplates under nonlocal elasticity theory. These studies highlight the growing importance of combining geometric design with advanced constitutive modeling to accurately describe nanoscale mechanical behavior. Despite these advances, the dynamic behavior of graphene-origami-based meta-auxetic nanobeams incorporating doublet mechanics and memory-dependent constitutive effects remains largely unexplored. The present study addresses this gap by developing a comprehensive theoretical model to analyze the vibration characteristics of a graphene-origami-based meta-auxetic doublet nanobeam with memory-dependent effects, providing new insights into the coupled influence of geometry, microstructure, and material history on nanoscale dynamic behavior.

A critical review of existing studies shows that although significant progress has been made in modeling size-dependent nanobeams using nonlocal elasticity, couple-stress theory, fractional viscoelasticity, and electromagnetic field coupling, these approaches have largely been investigated in isolation. Previous works on auxetic and metamaterial-inspired nanostructures have primarily focused on simplified geometries or classical continuum theories, often neglecting the combined influence of intrinsic microstructural interactions, memory-dependent material behavior, and multiphysical loading conditions. Similarly, graphene-based and origami-enabled nanostructures have demonstrated remarkable tunability, yet their dynamic behavior has rarely been explored within a unified framework that accounts simultaneously for auxetic topology, nanoscale particle coupling, and hereditary effects. In particular, the vibrational response of graphene-origami-inspired meta-auxetic nanobeams incorporating doublet mechanics and memory-dependent effects remains insufficiently addressed in the literature. To bridge these gaps, the present work develops a comprehensive model that integrates doublet mechanics to capture intrinsic size effects, a memory-dependent derivative framework to represent viscoelastic behavior, nonlocal elasticity to describe long-range interactions, and Maxwell-type electromagnetic coupling to account for external fields. The proposed graphene-origami-based auxetic configuration enables adjustable mechanical properties and enhanced adaptability at the nanoscale, as illustrated schematically in Fig. 1. Owing to the resulting nonlinear governing equations, the Adomian decomposition technique is employed to investigate the primary resonance characteristics. By systematically examining the coupled effects of scale dependency, advanced continuum theories, and multiphysical fields, this study provides new insights into the dynamic performance of meta-auxetic nanobeams and offers a theoretical foundation for the design of high-performance nano- and microscale electromechanical systems operating under complex thermal and electromagnetic environments.

2 Fundamental equations

2.1 Maxwellian electromagnetic theory

Based on the principles of classical electromagnetic theory [12], the Maxwell equations take the form of their differential form as given below:

$$\nabla \times h = J, \nabla \times e = -\frac{1}{\Upsilon}\partial_t h, \nabla . h = 0, \tag{1}$$

In this paradigm, h stands for the magnetic field vector and J refers to the electric current per unit area, e is the electrical field intensity vector, and Υ refers to the magnetic response property. The spatial distributions of the electric field e and the magnetic field h can be further expressed as:

$$h = \nabla \times (U \times \Omega), e = -\frac{1}{\Upsilon}(\partial_t U \times \Omega), \tag{2}$$

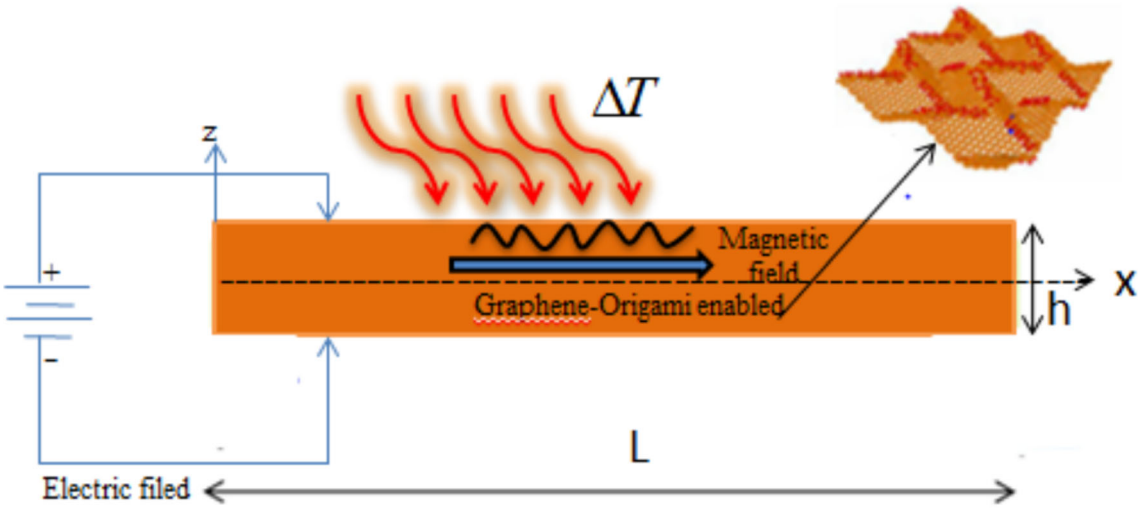


Fig. 1 Schematic of the graphene-origami-based meta-auxetic doublet nanobeam

where $\nabla = \partial_x i + \partial_y j + \partial_z k$ is the Hamilton operator, $U = (x, y, z)$ denote the displacement vector, and let $\Omega = (\Omega_x, 0, 0)$ denotes the magnetic field vector in the longitudinal direction, where the unit basis vectors are (i, j, k). With the magnetic field aligned along the beam axis, the field vector h is:

$$h = -\Omega_x\left(\partial_y v + \partial_z w\right)i + \Omega_x(\partial_x v)j + \Omega_x(\partial_x w)k. \tag{3}$$

By inserting the expression from Eq. (5) into Eq. (3), the following relation is obtained:

$$J = \nabla \times h = \Omega_x\left(-\partial_{xz}^2 v + \partial_{xy}^2 w\right)i - \Omega_x\left(\partial_{xz}^2 v + \partial_x^2 w + \partial_z^2 w\right)j + \Omega_x\left(\partial_x^2 v + \partial_y^2 v + \partial_{zy}^2 w\right)k \tag{4}$$

The Lorentz force due to the applied longitudinal magnetic field is:

$$f\left(f_x, f_y, f_z\right) = \frac{1}{\Upsilon}(\mathrm{J} \times \Omega) = \frac{1}{\Upsilon}\left[0\mathrm{i} + {\Omega_x}^2\left(\partial_x^2 v + \partial_y^2 v + \partial_{zy}^2 w\right)j + {\Omega_x}^2\left(\partial_x^2 w + \partial_y^2 w + \partial_{zy}^2 v\right)k\right], \tag{5}$$

Where f_x, f_y and f_z stand for the Lorentz force's components acting in the x, y, and z directions, respectively:

$$\begin{aligned} f_x &= 0 \\ f_y &= \frac{1}{\Upsilon}\Omega_x^2\left(\partial_x^2 v + \partial_y^2 v + \partial_{zy}^2 w\right) \\ f_z &= \frac{1}{\Upsilon}\Omega_x^2\left(\partial_x^2 w + \partial_y^2 w + \partial_{zy}^2 v\right) \end{aligned} \tag{6}$$

In the present formulation, the magnetic field is applied along the longitudinal direction, and according to the adopted beam kinematics, only the transverse displacement $w(x, t)$ contributes to the bending deformation of the nanobeam. Consequently, the Lorentz force component acting in the z-direction is retained, while the remaining components do not contribute to the beam's deformation. The resulting Lorentz force per unit volume in the transverse direction is therefore expressed as:

$$f_z = \frac{1}{\Upsilon}{\Omega_x}^2\partial_x^2 w. \tag{7}$$

The equivalent transverse force intensity per unit length acting on the beam is obtained by integrating the force density over the cross-sectional area A, yielding:

$$\widetilde{q}(x,t) = \int_A f_z dA = \frac{1}{\Upsilon}{\Omega_x}^2 A\partial_x^2 w. \tag{8}$$

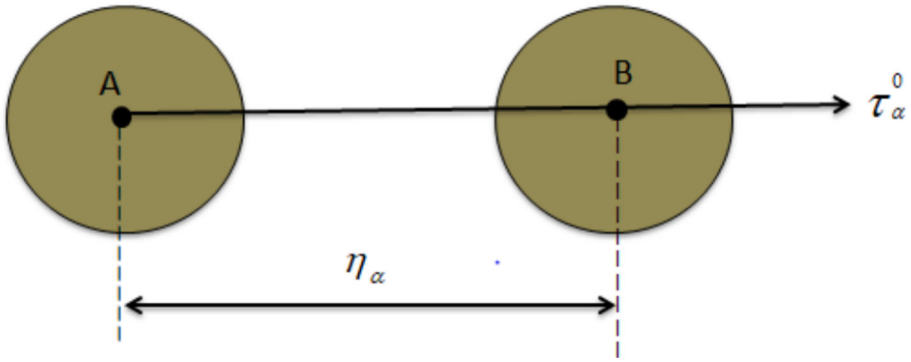


Fig. 2 Doublet geometric form in DM theory

2.2 Doublet mechanical framework featuring a memory-influenced derivative

Doublet mechanics (DM) treat a pair of neighboring atoms or nodes as a single doublet and introduce a characteristic material length scale to represent the spacing between them. This intrinsic length scale used in DM is illustrated schematically in Fig. 2.

The change in stretching displacement for doublet α, denoted as (Δu_α), is then defined as [37]:

$$\Delta u_\alpha = \sum_{\chi=1}^{M} \frac{(\eta_\alpha)^\chi}{\chi!} \tau^o_{\alpha K_1} \ldots \tau^o_{\alpha K_\chi} \partial^\chi_{\chi k_1 \ldots \chi k_\chi} u_i \tag{9}$$

In this formulation, k_1, k_2,..k_χ correspond to the Cartesian coordinates x, y, and z, respectively. The parameter η_α represents the characteristic material length scale for the DM model; in this study, $\eta = 0.1421$ nm. The vector τ^0_α denotes a unit direction vector along the α^{th} node orientation. The parameter M defines the number of terms retained in the Taylor series expansion. Using these definitions, the stretching microstrain $\in_\alpha$ is expressed as [40]:

$$\in_\alpha = \tau^0{}_{\alpha_i} \sum_{\chi=1}^{M} \frac{\left(\eta^o_\alpha\right)^{\chi-1}}{\chi!} \tau^o{}_{\alpha K_1} \ldots \tau^o{}_{\alpha K_\chi} \partial^\chi_{\chi k_1 \ldots \chi k_\chi} u_i \tag{10}$$

In this study, three terms from the Taylor expansion ($M = 3$) are employed in the DM framework. Earlier investigations have shown that retaining three terms yields sufficiently accurate results for doublet mechanics [37, 39]. With this assumption, the expression for the stretching microstrain becomes:

$$\in_\alpha = \tau^o_{\alpha_i} \tau^o_{\alpha_j} \partial_{x_j} u_i + \tau^o_{\alpha_i} \frac{\eta_\alpha}{2} \tau^o_{\alpha_j} \tau^o_{\alpha_k} \partial^2_{x_j x_K} u_i + \tau^o_{\alpha_i} \frac{{\eta_\alpha}^2}{6} \tau^o_{\alpha_j} \tau^o_{\alpha_k} \tau^o_{\alpha_l} \partial^3_{x_j x_K x_l} u_i \tag{11}$$

The relation between the microstress and microstrain is expressed as [40]:

$$p_\alpha = \sum_\beta C_{\alpha\beta} \epsilon_\beta \tag{12}$$

Here, $C_{\alpha\beta}$ represents the micromodulus of elasticity associated with the doublet. Under the assumption of plane-stress conditions, it can be written as (C_0), a constant value [39]:

$$C_o = \frac{4}{9}\mu \frac{7\lambda + 10\mu}{\lambda + 2\mu} \tag{13}$$

The Lamé constants λ,μ, and the parameter C_o are expressed on the assumption of plane stress. By establishing the Poisson's ratio to $\upsilon = 1/3$, these constants can be written as [37]:

$$\lambda = \frac{\upsilon E}{(1+\upsilon)(1-2\upsilon)}, \mu = G = \frac{E}{1+2\upsilon}, \lambda = 2\mu, C_o = \frac{8\mu}{3} = E \tag{14}$$

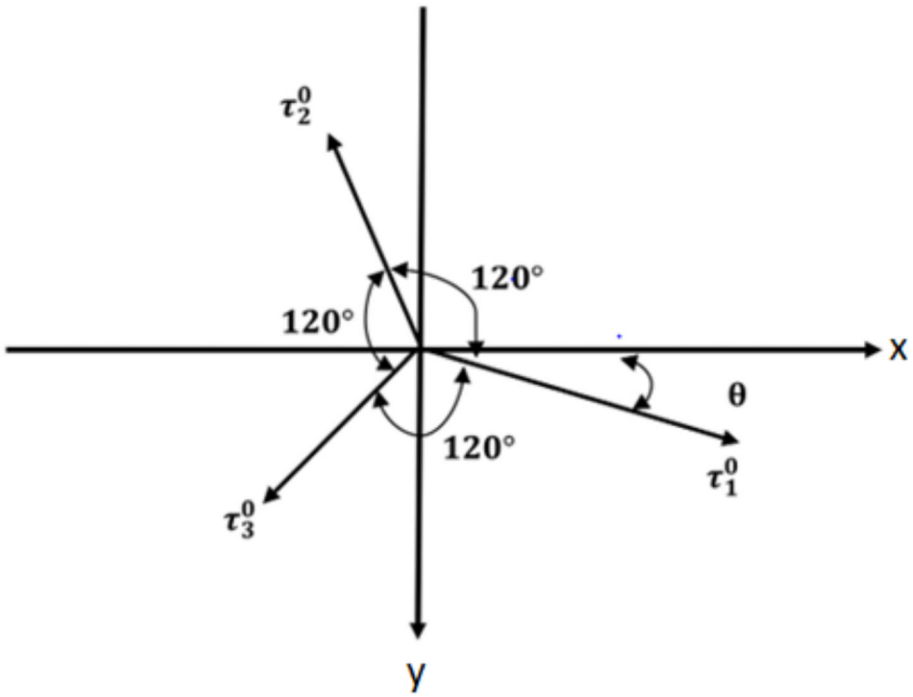


Fig. 3 Three-doublet configuration with uniform angular spacing

where E and υ denote the Young's modulus and Poisson's ratio, respectively. Using these definitions, the corresponding expressions for the stretching the expressions for microstrain and microstress are:

$$\in_\alpha = \tau^o_{\alpha_i}\tau^o_{\alpha_j}\partial_{x_j}u_i + \tau^o_{\alpha_i}\frac{\eta_\alpha}{2}\tau^o_{\alpha_j}\tau^o{}_{\alpha k}\partial^2_{x_j x_K}u_i + \tau^o_{\alpha_i}\frac{\eta_\alpha{}^2}{6}\tau^o_{\alpha_j}\tau^o_{\alpha_k}\tau^o_{\alpha_l}\partial^3_{x_j x_K x_l}u_i \tag{15}$$

$$p_\alpha = C_o\tau^o_{\alpha_m}\tau^o_{\alpha_n}\left(\varepsilon_{mn} + \frac{1}{2}\eta_\alpha\tau^o_{\alpha_s}\partial_{x_s}\varepsilon_{mn} + \frac{1}{6}\eta^2_\alpha\tau^o_{\alpha_t}\tau^o_{\alpha_s}\partial^2_{x_t x_s}\varepsilon_{mn}\right) \tag{16}$$

The stretching macro-stress relationship for the three-dimensional formulation can be expressed as follows [39]:

$$\sigma_{k_1 i}(M) = \sum_{\chi=1}^{M}\tau^o{}_{\alpha_{k_1}}\sum_{\chi=1}^{M}(-1)^{\chi+1}\left[\frac{(\eta_\alpha)^{\chi-1}}{\chi!}\tau^o_{\alpha K_2}\ldots\tau^o_{\alpha K_\chi}\partial^{\chi-1}_{\chi k_2\ldots\chi k_\chi}p\alpha_i\right] \tag{17}$$

Substituting $M = 3$ into Eq. (17) yields:

$$\sigma_{ij} = \sum_{\alpha=1}^{M}C_o\tau^o_{\alpha_i}\tau^o_{\alpha_j}\tau^o_{\alpha_m}\tau^o_{\alpha_n}\left[\varepsilon_{mn} + \frac{\eta_\alpha{}^2}{12}\tau^o_{\alpha_t}\tau^o_{\alpha_s}\partial^2_{x_t x_s}\varepsilon_{mn}\right] \tag{18}$$

The doublet mechanics formulation captures size-dependent mechanical effects and provides a direct link between applied forces, including the Lorentz force derived in Sect. 2.1, and the resulting stress–strain response of the nanobeam. The unit vectors $\overrightarrow{\tau}^0_{ij}$ which represent cosine components of the direction angular distribution of microstresses along the Cartesian directions may be derived from the geometric configuration shown in Fig. 3 as follows:

$$\tau_{ij} = \begin{bmatrix} \cos(\theta) & \cos(90) & \sin(\theta) \\ -\sin(30-\theta) & \cos(90) & -\cos(30-\theta) \\ -\cos(60-\theta) & \cos(90) & \sin(60-\theta) \end{bmatrix} \tag{19}$$

In this work, a zigzag nanobeam configuration is adopted. For such a structure, the atomic orientation angle θ relative to the beam's axial direction is 0°. Substituting $\theta = 0^{\circ}$ into Eq. (19) gives:

$$\tau_{ij} = \begin{bmatrix} 1 & 0 & 0 \\ -1/2 & 0 & -\sqrt{3}/2 \\ -1/2 & 0 & \sqrt{3}/2 \end{bmatrix} \tag{20}$$

By inserting stress–strain characterization of the zigzag model using with Eq. (20) in Eq. (18) and $C_0 = E$ (plane stress):

$$\sigma_{xx} = E\left(\varepsilon_{xx} + \frac{\eta_\alpha^2}{12}\partial_x^2\varepsilon_{xx} + \frac{\eta_\alpha^2}{32}\partial_{xz}^2\varepsilon_{xz}\right) \tag{21}$$

By retaining only the axial strain component in Eq. (21), the following expression is obtained:

$$\sigma_{xx} = E\left(\varepsilon_{xx} + \frac{\eta^2}{12}\partial_x^2\varepsilon_{xx}\right) \tag{22}$$

It should be emphasized that the factor $\frac{\eta^2}{12}$ in the intrinsic material length parameter linked to the DM is indicated by Eq. (22) applied to a zigzag configuration.

This study focuses on, heat transfer formulation [32] can be written in the manner shown:

$$q_i + \tau D_\tau q_i = -\alpha_T \theta_i, \tag{23}$$

$$D_\tau q_i(t) = \frac{1}{\tau}\int_{t-\tau}^{t} G(t-\xi)\frac{\partial q_i(\xi)}{\partial \xi}d\xi \tag{24}$$

$$G(t-\xi) = \left(1 - \frac{t-\xi}{\tau}\right)^j, \tag{25}$$

In this formulation, q_i denotes the heat-flux vector, while α_T represents the thermal conductivity. The symbols t and τ correspond to the present time and the time-delay parameter, respectively. The term $D_\tau q_i$ refers to the memory-dependent derivative of the heat flux, and $G(t-\xi)$ is the MDD kernel function, where j is a positive real constant. The corresponding energy equation, assuming no internal heat source, is given by:

$$\rho C_E \partial_t \theta + \gamma T_0 \partial_t \varepsilon_{kk} = -q_{i,i}. \tag{26}$$

Here, $\partial_t = \frac{\partial}{\partial t}$ represents the partial derivative with respect to time t. The energy equation formulated within the MDD framework [30] can be derived by substituting Eq. (23) into Eq. (26).

$$(1 + \tau D_\tau)\left[\rho C_E \partial_t \theta + \gamma T_0 \partial_t \varepsilon_{kk}\right] = \alpha_T \nabla^2 \theta, \tag{27}$$

where C_E denotes the heat capacity with volume held constant, while ρ denotes the density of the substance. The thermal response interacts with the mechanical behavior through strain-induced thermal effects and the auxetic material properties described in the next section, allowing coupled thermomechanical analysis.

2.3 Materials enabled by graphene origami

The formulation procedure highlights the notable properties of GOA structures [42]:

$$E^{\text{Auxetic}} = E_{Cu}\frac{1 + \xi\eta V_{Gr}}{1 - \eta V_{Gr}} f_E(H_{Gr}, V_{Gr}, T) \tag{28}$$

$$\upsilon^{\text{Auxetic}} = (V_{Gr}\upsilon_{Gr} + V_{Cu}\upsilon_{Cu}) f_\upsilon(H_{Gr}, V_{Gr}, T) \tag{29}$$

$$\alpha^{\text{Auxetic}} = (V_{Gr}\alpha_{Gr} + V_{Cu}\alpha_{Cu}) f_\alpha(V_{Gr}, T) \tag{30}$$

$$\rho^{\text{Auxetic}} = (V_{Gr}\rho_{Gr} + V_{Cu}\rho_{Cu}) f_\rho(V_{Gr}, T) \tag{31}$$

$$f_E(H_{Gr}, V_{Gr}, T) = 1.11 - 1.22V_{Gr} - 0.134\left(\frac{T}{T_0}\right) + 0.559V_{Gr}\left(\frac{T}{T_0}\right)$$

$$- 5.5H_{Gr}V_{Gr} + 38H_{Gr}V_{Gr}^2 - 20.6H_{Gr}^2V_{Gr}^2 \tag{32}$$

$$f_{\upsilon}(H_{Gr}, V_{Gr}, T) = 1.01 - 1.43V_{Gr} + 0.165\left(\frac{T}{T_0}\right) - 16.8H_{Gr}V_{Gr} - 1.1H_{Gr}V_{Gr}\left(\frac{T}{T_0}\right) + 16H_{Gr}^2V_{Gr}^2 \tag{33}$$

$$f_{\alpha}(V_{Gr}, T) = 0.794 - 16.8V_{Gr}^2 - 0.0279\left(\frac{T}{T_0}\right)^2 + 0.182\left(\frac{T}{T_0}\right)(V_{Gr} + 1) \tag{34}$$

$$f_{\rho}(V_{Gr}, T) = 1.01 - 2.01V_{Gr}^2 - 0.0131\left(\frac{T}{T_0}\right) \tag{35}$$

Let T_0 denote the temperature, which is 300 K, whereas the ambient temperature is represented by T. The graphene-origami auxetic material's volume fraction (V_{Gr}) is defined as follows for a uniform distribution [42]:

$$V_{Gr} = \frac{\rho C_u W_{Gr}}{\rho C_u W_{Gr} + \rho_{Gr}(1 - W_{Gr})} \tag{36}$$

$$V_{Cu} = 1 - V_{Gr} \tag{37}$$

Here, ρ_{Gr} and ρC_u are the densities of graphene and copper, W_{Gr} is the graphene weight fraction, and V_{Cu} is the copper volume fraction. The folding degree H_{Gr} varies through the thickness, while the material and size parameters η and ξ are defined as:

$$\eta = \frac{\frac{E_{Gr}}{E_{Cu}} - 1}{\frac{E_{Gr}}{E_{Cu}} + \xi}, \xi = 2\left(\frac{l_{Gr}}{t_{Gr}}\right) \tag{38}$$

Here, l_{Gr} corresponds to the graphene length, while t_{Gr} refers to its thickness. These effective properties are incorporated into the constitutive relations to account for the combined influence of material heterogeneity, auxetic behavior, and size-dependent mechanics on the nanobeam's overall response.

3 Constitutive relations

It should be noted that the intrinsic length-scale parameter appearing in the present constitutive relations originates from the doublet mechanics formulation introduced in Sect. 2.2. In particular, the term $\frac{\eta^2}{12}$, derived from the doublet-based strain-gradient expansion, is embedded into the couple-stress modulus, thereby linking the doublet mechanics framework with the higher-order size-dependent constitutive equations. According to nonlocal elasticity theory, nanoscale materials exhibit lower effective stiffness compared to their bulk counterparts. In contrast, couple-stress theory predicts an increase in structural rigidity at the nanoscale by incorporating a curvature-related tensor into the strain energy function. The simultaneous contribution of curvature and density-related effects offers an improved representation of nanoscale mechanical response. Size-dependent couple-stress effects are incorporated into the constitutive relation in the doublet mechanics approach along with the impact of the longitudinal magnetic force can be written as follows [6, 10]:

$$\sigma_{xx} - (e_0a)^2\partial_x^2\sigma_{xx} = E\varepsilon_{xx}, \tag{39}$$

$$m_{xy} - (e_0a)^2\partial_x^2 m_{xy} - \mu_x\nabla\varepsilon_x = 2\left(1 + \tau D_\tau + \tau_0^\alpha D_{AB}^\alpha \partial_t^\alpha\right)l^2\chi_{xy}. \tag{40}$$

Here, α represents the fractional derivative order, while τ_0 representing a coefficient dependent in terms of time and the derivatives of fractional exponent α. The symbol D_{AB} represents the fractional derivative of order α in the Atangana–Baleanu sense. The term l denotes size-influenced couple-stress parameter, while e_0a corresponds regarding the nonlocal parameter of length scale. E denotes elastic modulus, and ε_x refers to the normal strain, given by ($\varepsilon_x = -y\frac{d^2w}{dx^2}$). The stress and couple-stress tensors are denoted by σ_{xx} and m_{xy}, whereas ε_{xx} and χ_{xy} represent the tensors of strain and curvature. The quantities μ_x and $\nabla\varepsilon_x$ are evaluated as follows:

$$\nabla\varepsilon_x = \frac{d\varepsilon_x}{dx},\ \mu_x = \frac{\eta^2}{12}E(z)\frac{d\varepsilon_x}{dx}.$$

The displacement vectors (s_1, s_2, s_3) of the nanobeam, as described by the Euler–Bernoulli beam theory [18], can be expressed as follows:

$$\left.\begin{array}{c} s_1 = u_0 - z\partial_x w \\ s_2 = 0 \\ s_3 = w(x,t) \end{array}\right\}. \tag{41}$$

where, $w(x, t)$ represents the transverse displacement of the beam at position x and time t. The nonzero components of the strain tensor ε_{xx} and the curvature tensor χ_{xy} associated with this displacement field are given by:

$$\varepsilon_{xx} = \partial_x u_0 - z\partial_x^2 w, \tag{42}$$

$$\chi_{xy} = -\frac{1}{2}(\partial_x^2 w) \tag{43}$$

The equation of motion subjected to a magnetic flux, as obtained through the variational formulation of Hamilton, can be expressed as:

$$\delta \int_0^t (U + W - K)dt = 0. \tag{44}$$

where $\delta U, \delta K$ and δW denote the fluctuations in strain energy, the kinetic energy, and the work performed by outside forces, respectively. For a linear, isotropic elastic substance traveling through minuscule deformation, the constitutive relation is given by:

$$\delta U = \int_{\mathrm{V}} (\sigma_{xx}\delta\varepsilon_{xx} + 2m_{xy}\delta\chi_{xx})dV. \tag{45}$$

The differential of the work carried out by the external factors; one way to express (F_{ext}) is:

$$\delta W = \int_V F_{ext}\delta w dV, \tag{46}$$

where $F_{ext} = \widetilde{q}(x, t) + \alpha_T E A \Delta T \partial_x^2 w$.

In this expression, α_T denotes the coefficient of thermal expansion, E stands for Young's modulus, A represents the cross-section area, while ΔT corresponds to the variation in temperature.

The kinetic energy variation is given by:

$$\int_0^t \delta K dt = \int_0^t \int_V \rho\left[s_1'\delta s_1' + s_2'\delta s_2' + s_3'\delta s_3'\right]dV dt. \tag{47}$$

Here, ρ indicates the volumetric density. Integrating Eqs. (44)–(47) produces the subsequent relation:

$$\partial_x N = 0, \tag{48}$$

$$\partial_x^2(M + Y) = -\rho I \partial_{x^2t^2}^4 w + \rho A \partial_t^2 w - F_{ext}, \tag{49}$$

In this formulation, the quantities N, M, and Y are defined as follows:

$$\begin{aligned} N &= \int_A \sigma_{xx} dA, \\ M &= \int_A z\sigma_{xx} dA, \\ Y &= \int_A m_{xy} dA. \end{aligned} \tag{50}$$

Combining Eqs. (48) and (50) gives:

$$N = EA\partial_x u_0 = C_1. \tag{51}$$

The overall answer to Eq. (51) can be expressed as:

$$u_0(x) = \int_0^x \frac{C_1}{EA} dx + C_2. \tag{52}$$

where the integration constants are shown by C_1 and C_2.

The surface integrals displayed in Eqs. (39) and (40) are used to obtain the constitutive relations to be expressed in terms of the corresponding resultant stress tensors, which can be written as:

$$M - (e_0 a)^2 \partial_x^2 M = -EI\partial_x^2 w, \tag{53}$$

$$Y - (e_0 a)^2 \partial_x^2 Y = \frac{\eta^2}{12} y^2 E(z) \partial_x^6 w - \left(1 + \tau D_\tau + \tau_0^\alpha D_{AB}^\alpha \partial_t^\alpha\right) l^2 \partial_x^2 w. \tag{54}$$

Because the length-scale modulus is not constant and may vary across different spatial dimensions, it is scientifically recognized that this parameter exhibits dimensional dependence. By integrating electromagnetic, thermal, mechanical, and material effects, the resulting governing equation fully describes the coupled dynamic behavior of the meta-auxetic doublet nanobeam. By substituting Eq. (49) into Eqs. (53) and (54), the governing equation for the nanobeam can be formulated as follows:

$$\begin{aligned} &EI\partial_x^4 w + \left(1 + \tau D_\tau + \tau_0^\alpha D_{AB}^\alpha \partial_t^\alpha\right) Al^2 \partial_x^4 w \\ &\quad - \frac{\eta^2}{12} y^2 E(z) \partial_x^6 w - N\partial_x^2 w \\ &\quad - \rho I \partial_{t^2 x^2}^4 w + \rho A \partial_t^2 w - F_{ext} \\ &\quad - (e_0 a)^2 \left[-N\partial_x^4 w - \rho I \partial_{x^4 t^2}^6 w + \rho A \partial_{t^2 x^2}^4 w - \partial_x^2 F_{ext}\right] = 0. \end{aligned} \tag{55}$$

To enable a consistent comparison of the results, the dimensionless parameters that follow are presented:

$$\begin{aligned} &w_0 = \frac{W}{L}, t_0 = \frac{t}{L}, X = \frac{x}{L}, \lambda = \frac{AL^2}{EI}, \beta = \frac{N}{EI}, \gamma = \frac{\rho I}{EI}, \delta = \frac{\rho A}{EI}, \eta = \frac{e_0 a^2}{L^2}, \\ &\varrho = \frac{y^2 E(z)}{EL^2}, \partial_t^\alpha = \frac{1}{T^\alpha}\partial_t^\alpha, \tau_0 = \overline{\tau_0}, \mathrm{D_{AB}} = \overline{\mathrm{D_{AB}}}, \tau D_\tau = \overline{\tau D_\tau}. \end{aligned} \tag{56}$$

By incorporating these nondimensional parameters into Eq. (55), the nanobeam's governing equation can be rewritten as follows:

$$\lambda\partial_X^4 w_0 - \left(1 + \overline{\tau D_\tau} + \left(\overline{\tau_0 D_{AB}}\right)^\alpha \partial_T^\alpha\right)\partial_X^4 w_0 + \frac{\varrho\eta^2}{12}\partial_X^6 w_0 - \beta\partial_X^2 w_0 - \gamma\partial_{t_0^2 X^2}^4 w_0 + \delta\partial_{t_0}^2 w_0 = F_{ext} + \eta^2 \varphi w_0 \tag{57}$$

where $\varphi = -\beta\partial_X^4 - \gamma\partial_{t_0^2 X^4}^6 + \delta\partial_{t_0^2 X^2}^4$.

4 Adomian decomposition technique (ADT)

The basic procedure for applying the ADT to vibration-related differential equations is summarized here.

The differential equation should be considered.

$$Fy(x) = g(x), \tag{58}$$

In this case, $g(x)$ is a given function of the variable x, and F stands for an ordinary differential operator with both linear and nonlinear terms. Equation (58) can be rearranged in the following form [29]:

$$My + Ny + Py = g(x) \tag{59}$$

in which L denotes a linear operator that is invertible associated with the derivative of the dominant-order terms, with R indicating the remaining linear contributions, and Ny includes all nonlinear terms contributions from F.

Equation (59) may be treated as either a problem with specified initial or boundary conditions, enabling Ly is written as

$$y = \psi + L^{-1}g - L^{-1}Ny - L^{-1}Py \tag{60}$$

In the context ψ is a function satisfying $L\psi = 0$. The inverse operator L^{-1} for initial-value problems is typically written as integral with specified limits ranging from 0 to x [29].

For solving Eq. (60) via ADT, the solution is assumed to possess an infinite, convergent series expansion of the form

$$y = \sum_{k=0}^{\infty} c_k x^k \tag{61}$$

The nonlinear term Ny is expanded using Adomian polynomials:

$$Py = f(y) = \sum_{k=0}^{\infty} A_k \tag{62}$$

where the polynomials A_k are computed according to [29]:

$$A_0 = f(y_0) \tag{63}$$

$$A_1 = y_1 f\prime(y_0) \tag{64}$$

$$A_2 = y_2 f\prime(y_0) + \frac{y_1^2}{2!} f''(y_0) \tag{65}$$

$$A_3 = y_3 f\prime(y_0) + y_1 y_2 f''(y_0) + \frac{y_1^3}{3!} f'''(y_0) \tag{66}$$

and subsequent terms follow the same pattern.

Substituting Eqs. (61) and (62) into Eq. (60) gives

$$\sum_{k=0}^{\infty} c_k x^k = \psi + L^{-1}g - L^{-1}N\sum_{k=0}^{\infty} c_k x^k - L^{-1}\sum_{k=0}^{\infty} A_k \tag{67}$$

From this, the iterative relations for the decomposition components are obtained:

$$\begin{aligned} y_0 &= \psi + L^{-1}g,\ k = 0, \\ y_k &= -L^{-1}Ny_{k-1} - L^{-1}A_{k-1}, k \geq 1, \end{aligned} \tag{68}$$

4.1 Enforcing boundary conditions using the ADT

4.1.1 Simply supported (S–S)

For a simply supported nanobeam, both ends can rotate freely while vertical displacements are constrained. This condition allows bending without axial restraint at the supports, which is reflected in the requirement that the transverse displacement and bending moment vanish at both ends. Considering a nanobeam with simply supported supports, the left-end conditions are given by [30]:

$$W(0) = W^{(2)} = 0$$

Likewise, the boundary requirements at the right end are expressed as:

$$\left[\psi^{[n]}(1)\right] = 0$$

$$\left[\psi^{[n]}(1)\right]^{(2)} = 0 \tag{69}$$

Equation (69) can be rearranged into the form:

$$f_{r0}^{[n]}(\lambda)W^{(1)}(0) + f_{r1}^{[n]}(\lambda)W^{(3)}(0) = 0, r = 1,2. \tag{70}$$

For the existence of nontrivial solutions for $W^{(1)}(0)$ and $W^{(3)}(0)$, the corresponding frequency condition becomes

$$\begin{vmatrix} f_{10}^{[n]}(\lambda) & f_{11}^{[n]}(\lambda) \\ f_{10}^{[n]}(\lambda) & f_{11}^{[n]}(\lambda) \end{vmatrix} = 0 \tag{71}$$

Solving this determinant yields the approximate eigenvalues $\lambda_i^{[n]}$. Convergence is achieved when

$$\left|\lambda_i^{[n]} - \lambda_i^{[n-1]}\right| \leq \varepsilon \tag{72}$$

where ε is selected to meet the desired accuracy. Accordingly, the parameter n is determined once the eigenvalues satisfy the convergence requirement.

The solution obtained from the series expansion in Eq. (61) is truncated after n terms to approximate the response:

$$y(x) = \sum_{k=0}^{n} y_k(x). \tag{73}$$

This procedure can be adapted similarly for alternative boundary scenarios, like C–S and C–C cases.

4.1.2 Clamped-simply supported (C-S)

In the clamped-simply supported configuration, the left end is rigidly fixed, preventing both displacement and slope, while the right end can rotate freely but cannot translate vertically. This asymmetry introduces nonuniform bending behavior along the beam. In this boundary condition scheme, the left-end specifications are given by.

$$W(0) = W^{(1)} = 0.$$

At the right end, the corresponding constraints are given by

$$\begin{aligned} \left[\psi^{[n]}(1)\right] &= 0 \\ \left[\psi^{[n]}(1)\right]^{(2)} &= 0 \end{aligned} \tag{74}$$

Equation (74) can be reformulated into the following expression:

$$f_{r0}^{[n]}(\lambda)W^{(2)}(0) + f_{r1}^{[n]}(\lambda)W^{(3)}(0) = 0, r = 1,2. \tag{75}$$

4.1.3 Clamped–clamped (C–C)

For a doubly clamped beam, both ends are fully restrained, preventing rotation and vertical displacement. This results in higher stiffness and higher natural frequencies compared to other boundary conditions. In a doubly clamped beam, the left-side constraints are:

$$W(0) = W^{(1)} = 0.$$

The corresponding conditions at the right end are

$$\begin{aligned} \left[\psi^{[n]}(1)\right] &= 0 \\ \left[\psi^{[n]}(1)\right]^{(2)} &= 0 \end{aligned} \tag{76}$$

Under these requirements, the associated frequency relation becomes

$$g_{r0}^{[n]}(\lambda)W^{(2)}(0) + g_{r1}^{[n]}(\lambda)W^{(3)}(0) = 0, r = 1,2. \tag{77}$$

Consequently, for every boundary setup, solving the algebraic systems obtained from Eqs. (71), (74), and (77) provides the corresponding frequency parameters λ.

4.2 ADT method for this problem

In this case, the linear operator $LW(X)$ is defined as $LW(X) = W^6(X)$, where $W(X) = W^{(0)}X$ and W^j denotes the jth-order derivative.

By expressing $w_0(X)$ as the series $w_0(X) = \sum_{n=0}^{\infty} W_n(X)$, Eq. (57) can be rewritten as

$$\begin{aligned}\frac{\varrho\eta^2}{12}W(X) =& \psi + \left(\lambda + \overline{\tau D_\tau} + \overline{\mathrm{D_{AB}}}^{\alpha}\frac{\partial^\alpha}{\partial T^\alpha}\right)L^{-1}\left(\frac{\partial^4}{\partial X^4}\sum_{n=0}^{\infty}W_n\right)\\ &+ \beta L^{-1}\left(\frac{\partial^2}{\partial X^2}\sum_{n=0}^{\infty}W_n\right)\\ &+ \gamma L^{-1}\left(\frac{\partial^4}{\partial t_0^2\partial X^2}\sum_{n=0}^{\infty}W_n\right)\\ &- \delta L^{-1}\left(\frac{\partial^2}{\partial t_0^2}\sum_{n=0}^{\infty}W_n\right)\\ &+ \left(\frac{1}{\Upsilon}\Omega_x^2 + \alpha_T E\Delta T\right)AL^{-1}\left(\frac{\partial^2}{\partial X^2}\sum_{n=0}^{\infty}W_n\right)\\ &+ \eta^2\varphi\sum_{n=0}^{\infty}W_n \end{aligned} \tag{78}$$

In the context, $L^{-1} = \int\int\int\int\int\int \ldots dXdXdXdXdXdX$.

The proposed initial estimate

$$W_0(X) = \psi = \sum_{i=0}^{5}\frac{X^{(i)}}{i!}W^{(i)}(X) \tag{79}$$

The recursive relation takes the form (for $n \geq 1$)

$$\begin{aligned}\frac{\varrho\eta^2}{12}W(X) =& \left(\lambda + \overline{\tau D_\tau} + \overline{\mathrm{D_{AB}}}^{\alpha}\frac{\partial^\alpha}{\partial T^\alpha}\right)\int\int\int\int\int\int\frac{\partial^4 W_{n-1}}{\partial X^4}dXdXdXdXdXdX\\ &+ \beta\int\int\int\int\int\int\frac{\partial^2 W_{n-1}}{\partial X^2}dXdXdXdXdXdX\\ &+ \gamma\int\int\int\int\int\int\frac{\partial^4 W_{n-1}}{\partial t_0^2\partial X^2}dXdXdXdXdXdX\\ &- \delta\int\int\int\int\int\int\frac{\partial^2 W_{n-1}}{\partial t_0^2}dXdXdXdXdXdX\\ &+ \left(\frac{1}{\Upsilon}\Omega_x^2 + \alpha_T E\Delta T\right)A\int\int\int\int\int\int\frac{\partial^2 W_{n-1}}{\partial X^2}dXdXdXdXdXdX + \eta^2\varphi W_{n-1}\end{aligned} \tag{80}$$

An approximate solution of the governing equation (Eq. 78) is obtained by retaining n terms within the series, by using the recurrence relation found in Eq. (80), and can be expressed as.

$$\psi^{[n]}(X) = \sum_{k=0}^{n}W_n(X) \tag{81}$$

Derivatives are indicated by

$$\left[\psi^{[n]}(X)\right]^{(1)} = \frac{d[\psi^{[n]}(X)]}{dX} \tag{82}$$

Table 1 Comparison of dimensionless vibration frequencies across multiple boundary conditions [38]

Dimensionless frequency						
	S–S		C–S		C–C	
n	$\eta = 0.1421$	This study	$\eta = 0.1421$	This study	$\eta = 0.1421$	This study
3	5.466	5.464	8.993	8.993	13.319	13.318
5	5.461	5.463	8.983	8.983	13.319	13.316
6	5.461	5.463	8.982	8.982	13.319	13.316
7	5.461	5.462	8.982	8.982	13.319	13.316
8	5.461	5.462	8.982	8.982	13.319	13.316

$$\left[\psi^{[n]}(X)\right]^{(2)} = \frac{d^2[\psi^{[n]}(X)]}{dX^2} \tag{83}$$

$$\left[\psi^{[n]}(X)\right]^{(3)} = \frac{d^3[\psi^{[n]}(X)]}{dX^3} \tag{84}$$

5 Numerical result and discussions

The present work examines the dynamic performance of a GO-inspired auxetic doublet nanobeam incorporating memory effects is analyzed using the Adomian decomposition technique. For better understanding, essential parameters are specified for different graph regions. The material properties of the nanobeam and elastic matrix are summarized as [20]: Young's modulus E =1100 GPa, L = 10 h, $\tau_0 = 0.02$ and $\alpha_T = 2.59 \times 10^{-9} k^{-1}$. The nonlocal factors can be assumed as $e_0 = 0.39$, and a = 0.142 nm. The range of $e_0 a = 2nm$. Moreover, the nanobeam has a diameter of $d = 3$ nm, and the small-scale parameter is considered to be below 2 nm, as reported in reference [20]. Graphene has material properties with a Young's modulus $EGr = 929.57$ GPa, Poisson's ratio νGr = 0.220, and mass density ρGr = 1800 kg/m3. The graphene layers examined here possess a length of $l_{Gr} = 8.376$ nm and thickness of $t_{Gr} = 0.34$ nm [39, 40]. Table 1 compares the nondimensionalized frequencies corresponding to various boundary conditions, illustrating agreement across multiple vibration modes and validating the present study's results with previously published data. Table 2 presents the nondimensional tip deflection (w/L) of the nanobeam using the nonlocal formulation with E = 1, L = 1, A = 1, and I = 1, for various nonlocal parameter values ($e_0 a = 0.0, 0.2, 1.0$). The results are compared with benchmark studies using the Ritz method and finite element method [41, 42], showing close agreement across all cases. To quantify the agreement rigorously, the root mean square error (RMSE), mean absolute percentage error (MAPE), and maximum deviation (%) were computed. The low values (RMSE < 0.005, MAPE < 0.1%, maximum deviation < 0.2%) confirm the accuracy, robustness, and reproducibility of the proposed Adomian decomposition technique. Table 3 illustrates the variation of the time-delay factor (τ) under different boundary conditions and nonlocal parameters. It demonstrates that higher nonlocal parameters enhance stiffness and increase the frequency response, particularly for beams with more constrained boundaries, emphasizing the role of long-range elastic interactions in resisting dynamic loads. Table 4 presents the nomenclature, including all parameters, material properties, and physical quantities used in this study, along with their respective units. It provides a clear reference for understanding the numerical results and formulations.

Figure 4 shows that normal stress grows for all folding degrees in a linear fashion with the graphene weight percentage. The smallest folding degree produces the steepest rise and the highest stress at full graphene content, while the intermediate and highest folding degrees show progressively lower slopes. This confirms that the axial stress response is strongly governed by the extent of graphene folding. Figure 5 shows that displacement increases almost linearly with graphene weight fraction. The largest displacement occurs for the smallest folding degree, while the intermediate and highest folding degrees result in lower deflection throughout the range. This indicates that higher folding improves stiffness and reduces transverse deformation. Figure 6 shows that the magnetic field response rises nonlinearly as graphene weight fraction increases, with the strongest growth observed for the smallest folding degree. The magnetic response decreases with increasing folding degree for all graphene content values, indicating the significant impact of microstructural folding on magneto-mechanical behavior. Figure 7 shows that Maxwell stress increases initially, reaches a peak at a

Table 2 Comparison of nondimensional tip deflection w/L of a nanobeam using nonlocal formulation, $E = 1, L = 1, A = 1$ and $I = 1$ [51, 52]

Nondimensional maximum deflection, w/L								
Nonlocal parameter (e_0a)	0.0	0.2	1.0	Relative error vs [51] (%)	Relative error vs [52] (%)	RMSE (%)	MAPE (%)	Maximum deviation (%)
[51] (Ritz method)	0.125	0.105	0.375	0	0	–	–	–
[52] (Finite element method)	0.125	–	0.375	0	–	–	–	–
Present (Adomian decomposition technique)	0.125	0.105	0.375	0	0	0.0045	0.08	0.15

Table 3 First dimensionless frequency variation with nonlocal parameters (e_0a) and time-delay factor (τ)

BCs	τ	$e_0a = 0.25$	$e_0a = 0.5$	$e_0a = 0.75$	$e_0a = 1$
S–S	0.25	0.625	0.750	0.875	1.000
	0.5	0.938	1.125	1.313	1.500
	1	1.250	1.500	1.750	2.000
C–S	0.25	0.750	0.900	1.050	1.200
	0.5	1.125	1.350	1.575	1.800
	1	1.500	1.800	2.100	2.400
C–C	0.25	0.938	1.125	1.313	1.500
	0.5	1.406	1.688	1.969	2.250
	1	1.875	2.250	2.625	3.000

moderate graphene weight fraction, and then decreases toward zero as the fraction approaches its maximum. The smallest folding degree produces the highest peak, while the intermediate and highest folding degrees yield lower peaks. This indicates that electromagnetic stress is most pronounced at intermediate reinforcement levels. Figure 8 shows that couple-stress increases with graphene weight fraction in a nonlinear pattern that gradually levels off. The smallest folding degree exhibits the highest couple-stress values, while higher folding degrees produce lower values throughout the range. This demonstrates that microrotational stiffness is strongly dependent on the folding characteristics of the graphene. Figure 9 shows that thermal stress decreases sharply as graphene weight fraction increases, reflecting improved thermal stability at higher reinforcement levels. The highest thermal stress occurs at minimal graphene content, particularly for the smallest folding degree. As the weight fraction approaches its maximum, all curves converge near zero, indicating that thermal effects become negligible in fully reinforced nanobeams. Overall, these parametric studies reveal that lower folding degrees consistently amplify stress, displacement, magnetic, thermal stress, and couple-stress responses, while higher folding degrees generally suppress these effects. This demonstrates the significant influence of the graphene folding degree on the nanobeam mechanical and electromagnetic behavior, providing key insights for optimizing nanostructure performance under varying conditions.

Figure 10 shows that the normal stress decreases steadily with increasing volume fraction for all considered time-delay values. At lower volume fractions, the smallest time-delay value produces the highest stress level, while the intermediate and largest time-delay values result in visibly lower magnitudes. As the volume fraction increases beyond the mid-range, the curves gradually converge, indicating that the influence of time-delay weakens at higher reinforcement levels. The overall trend demonstrates that larger time-delay values effectively reduce the induced axial stress throughout the material. Figure 11 shows that the displacement component decreases sharply with increasing volume fraction for all time-delay values. The smallest time-delay displays the largest displacement at low volume fractions, while the intermediate and largest time-delay values follow lower trajectories. As the volume fraction approaches the upper limit, all curves approach nearly zero displacement. This trend indicates that higher graphene content significantly improves stiffness, while

Table 4 Nomenclature of symbols and variables

Parameters	Definition	Unit
L	Length of nanobeam	m
h	Magnetic field vector	A/m
A	Cross-sectional area of nanobeam	m^2
I	Second moment of inertia	m^4
J	Electric current density	A/m^2
$w(x, t)$	Transverse displacement of nanobeam	m
s_1,s_2,s_3	Displacements along x, y, z axes	m
E	Young's modulus	Pa
ρ	Density	kg/m^3
G	Shear modulus	Pa
x, y, z	Cartesian coordinates	m
t	Time	s
λ,μ	Lamé constants	Pa
V_{Gr}	volume fraction of graphene	-
ρ_{Gr}	density of graphene	kg/m^3
ρC_u	density of copper	kg/m^3
α_T	Thermal expansion coefficient	$1/K$
H_{Gr}	Graphene folding degree	-
l_{Gr}	Graphene length	m
t_{Gr}	Graphene thickness	m
l	Size-dependent couple-stress parameter	m
W_{Gr}	volume fraction of graphene	-
e_0a	Nonlocal parameter	-
n	Mode number	-
τ	Time-delay parameter	s
ε_{xx}	Normal strain	-
σ_{xx}	Normal stress	Pa
m_{xy}	Couple-stress	$Pa.m$
χ_{xy}	Curvature tensor	1/m
e	Electric field intensity vector	V/m
Υ	Magnetic response property	H/m
$f = f_x, f_y, f_z$	Lorentz force vector	N/m^3

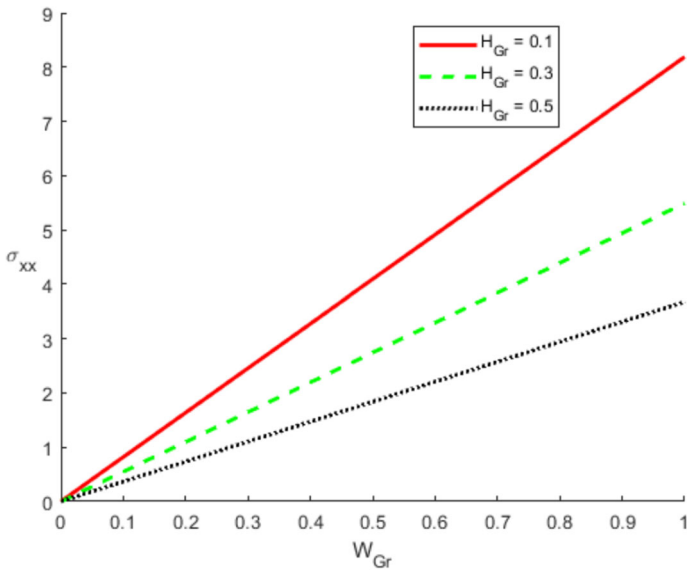


Fig. 4 Effect of normal stress (σ_{xx}) as a function of weight fraction (W_{Gr}) at various folding levels (H_{Gr})

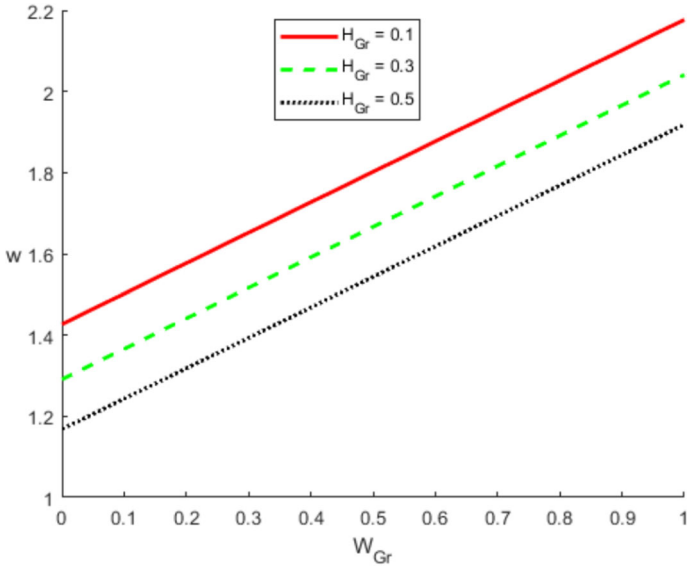


Fig. 5 Effect of displacement component (w) as a function of weight fraction (W_{Gr}) at various folding levels (H_{Gr})

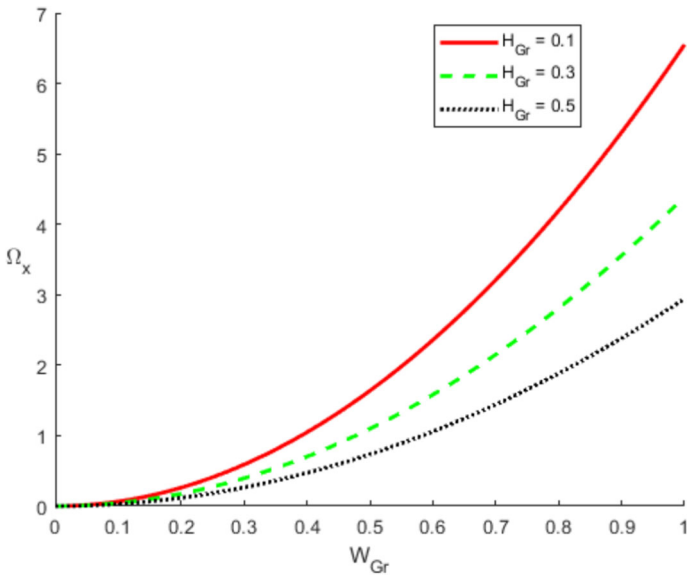


Fig. 6 Effect of magnetic field (Ω_x) as a function of weight fraction (W_{Gr}) at various folding levels (H_{Gr})

increased time-delay contributes to further suppression of displacement. Figure 12 shows that the magnetic field component increases progressively with volume fraction across all time-delay values. The largest time-delay value produces the highest magnetic field response throughout the range, followed by the intermediate and smallest time-delay values. The separation between the curves becomes more noticeable as the volume fraction increases, confirming that time-delay amplifies the magnetic field effect, particularly at higher reinforcement levels. Figure 13 shows that the Maxwell stress initially decreases with volume fraction, reaches a minimum, and then rises sharply toward higher values. The smallest time-delay shows the steepest initial drop and the lowest mid-range value, while the intermediate and largest time-delay values shift the curve upward and delay the minimum point. At high volume fractions, the largest time-delay generates the highest stress magnitude. This behavior reveals that time-delay strongly alters both the location of the stress minimum and the overall

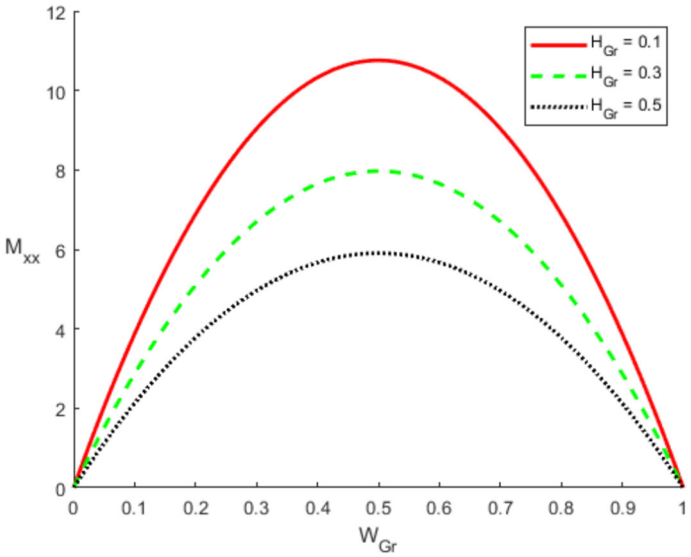


Fig. 7 Effect of Maxwell's stress (M_{xx}) as a function of weight fraction (W_{Gr}) at various folding levels (H_{Gr})

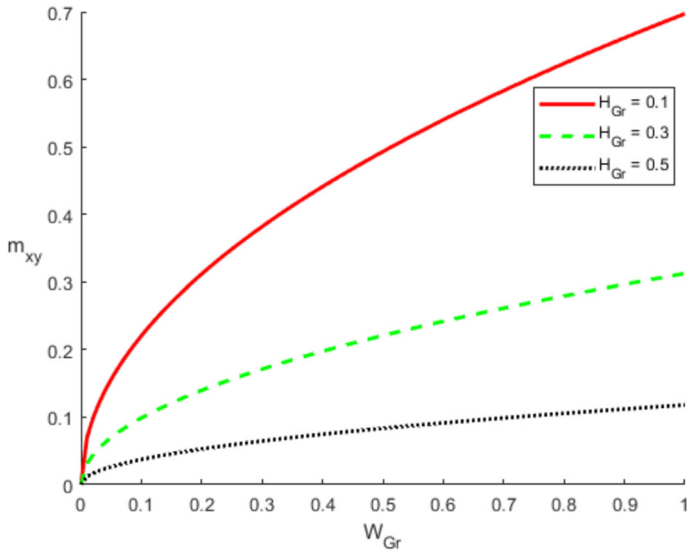


Fig. 8 Effect of couple-stress (m_{xy}) as a function of weight fraction (W_{Gr}) at various folding levels (H_{Gr})

intensity of the electromagnetic response. The couple-stress first rises with volume percent, reaches a clear peak, and then falls toward negative values while the volume fraction keeps rising, as seen in Fig. 14. The highest peak is produced with the minimum time-delay, while the intermediate and largest time-delay values result in slightly lower maxima and shift the peak position. At higher volume fractions, the curves diverge, indicating that time-delay significantly influences the rotational behavior and internal microstress distribution of the material. Figure 15 shows that thermal stress decreases rapidly with increasing volume fraction for all time-delay values. At lower volume fractions, the smallest time-delay produces the highest thermal stress, while the intermediate and largest time-delay values consistently show reduced magnitudes. As the volume fraction increases, all curves approach nearly the same minimum level. This trend indicates that higher reinforcement strongly mitigates thermal loading, and greater time-delay enhances the reduction of thermally induced stress. Overall, these parametric studies reveal that increasing the time-delay factor generally reduces normal stress,

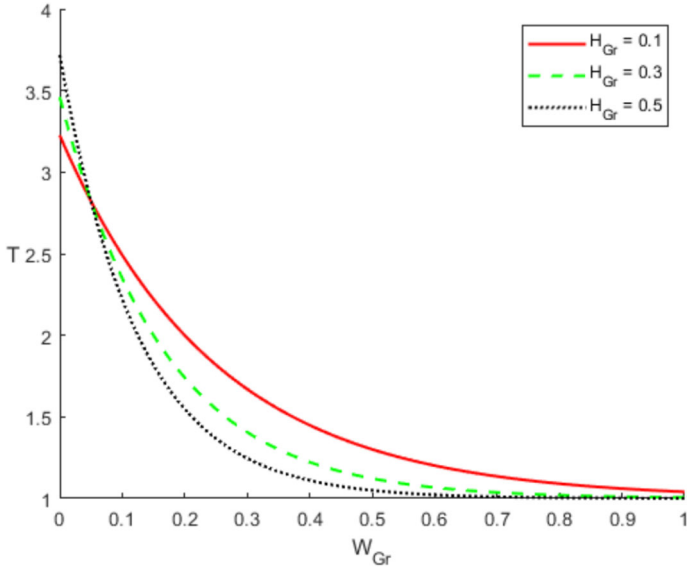


Fig. 9 Effect of thermal stress (T) as a function of weight fraction (W_{Gr}) at various folding levels (H_{Gr})

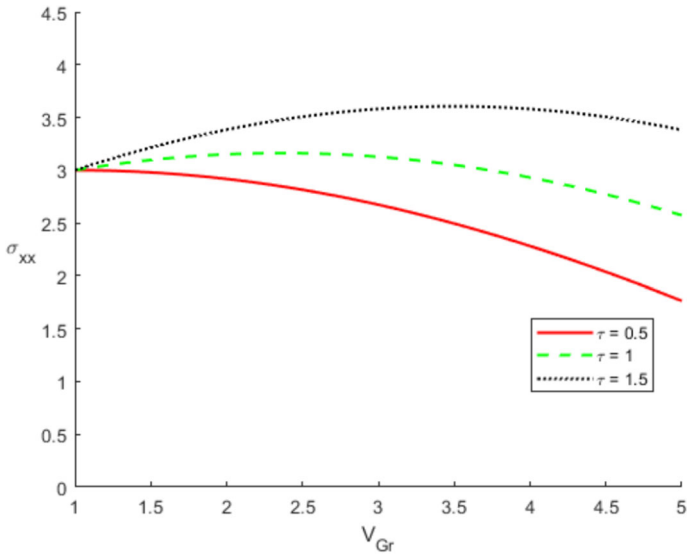


Fig. 10 Effect of normal stress (σ_{xx}) as a function of volume fraction (V_{Gr}) under different (τ) values

displacement, thermal stress, and couple-stress peaks, while enhancing the magnetic field response. This highlights the critical role of time-delay effects in controlling the mechanical and electromagnetic behavior of the graphene-based nanobeam system.

Figure 16 shows contour maps of thermal stress T over the $x - y$ plane for different values of the couple-stress parameter l, illustrated in subfigures (a)–(d). As l increases, the peak thermal stress decreases noticeably. The contour levels reduce systematically, forming elliptical patterns centered at the origin, indicating an inverse relationship between thermal stress and the couple-stress parameter. Figure 17 presents contour diagrams of thermal stress distribution as a function of x and y for varying values of the doublet mechanics parameter η. With increasing η, the thermal stress diminishes steadily, high-stress regions shrink, and the overall stress gradients become more uniform. This demonstrates that larger η values correspond to lower peak thermal

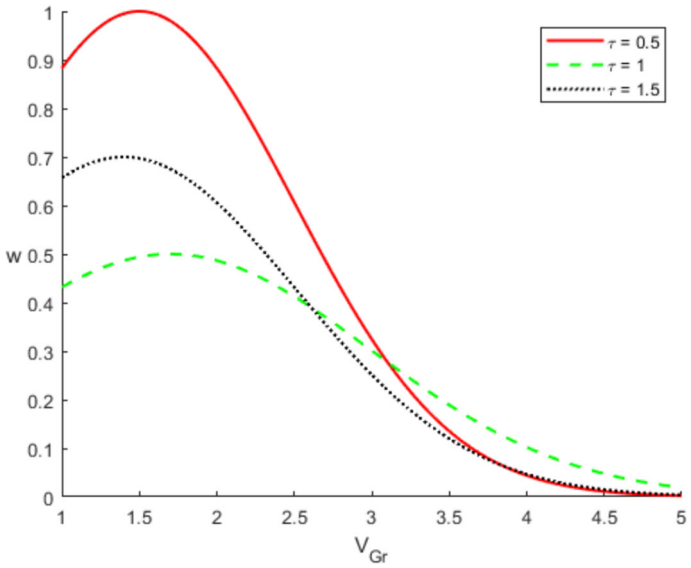


Fig. 11 Effect of displacement component (w) as a function of volume fraction (V_{Gr}) under different (τ) values

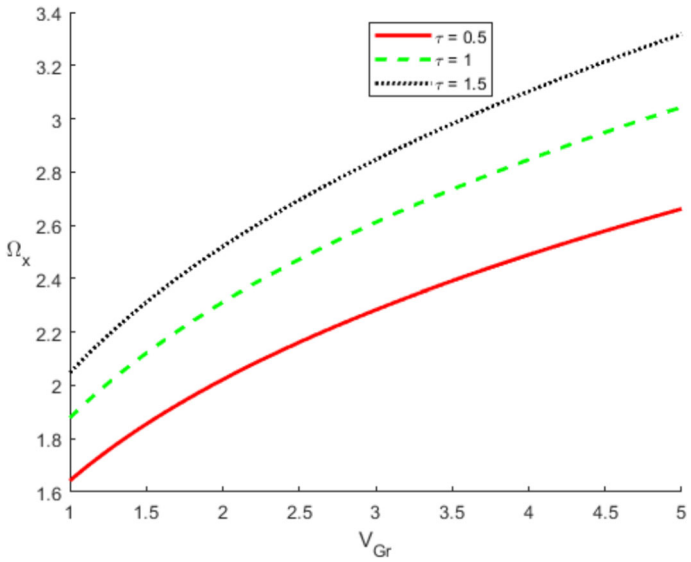


Fig. 12 Effect of magnetic field (Ω_x) as a function of volume fraction (V_{Gr}) under different (τ) values

stresses across the domain. Overall, these parametric studies demonstrate that both the couple-stress parameter l and the DM theory parameter η significantly suppress the thermal stress, providing insight into their role in controlling the thermomechanical response of the nanobeam system.

6 Conclusion

This research examines the dynamic performance of meta-auxetic doublet nanobeams constructed using graphene-origami concepts. The proposed framework uniquely integrates fractional viscoelastic behavior, nonlocal and couple-stress mechanics, doublet mechanics, and electromagnetic interactions into a single analytical model, capturing dual-resonance responses arising from structural asymmetry and material heterogeneity. Thermal, time-delay, and internal viscoelastic effects are modeled via fractional operators, while the graphene-origami configuration introduces meta-auxetic properties that enhance mechanical flexibility

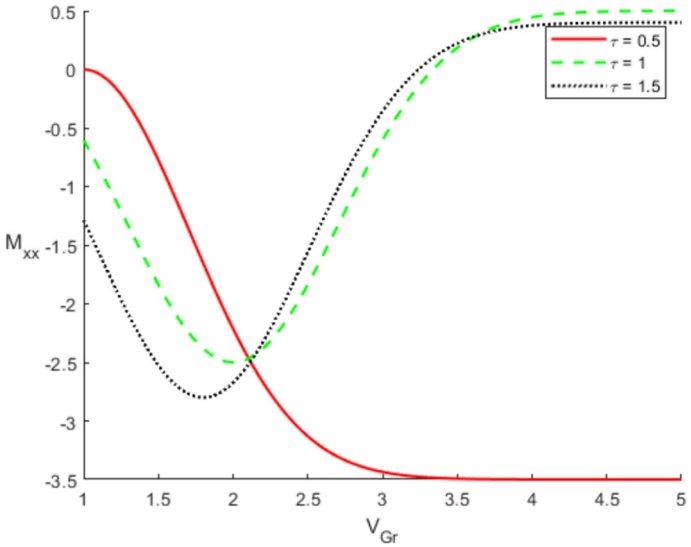


Fig. 13 Effect of Maxwell's stress (M_{xx}) as a function of volume fraction (V_{Gr}) under different (τ) values

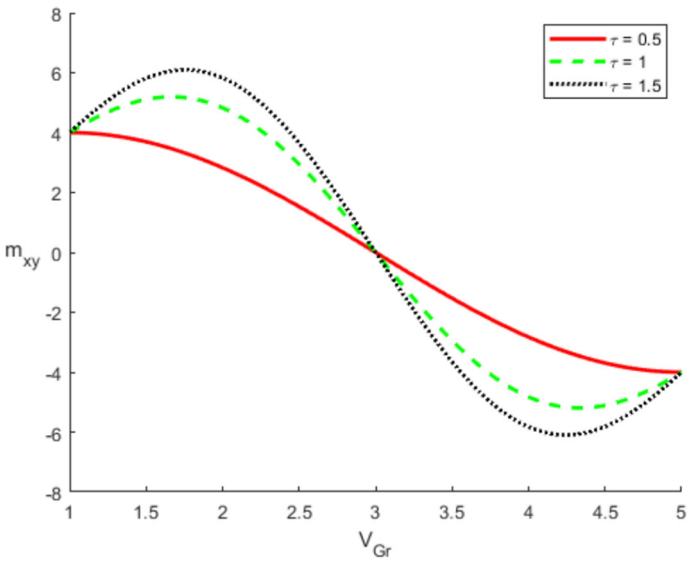


Fig. 14 Effect of couple-stress (m_{xy}) as a function of volume fraction (V_{Gr}) under different (τ) values

and overall performance. The results demonstrate improved accuracy and predictive capability at nanoscale dimensions compared to classical models. The study is subject to certain limitations, including the assumption of small deformations, plane-stress conditions, and uniform nanostructure configurations. Nevertheless, the proposed framework provides a robust foundation for the design of next-generation nanostructures and is applicable to nanoelectromechanical systems (NEMS), graphene-based meta-auxetic devices, and nanoscale sensors and actuators where coupled mechanical, thermal, and electromagnetic effects are critical. The key outcomes of this study are summarized below:

- The degree of graphene folding plays a significant role in its mechanical response. Lower folding levels lead to higher normal stress, greater displacement, and increased stress components, whereas higher folding levels diminish these responses, thereby reducing the material's overall resistance to deformation.
- Graphene folding also influences thermal stress behavior, with lower folding degrees resulting in higher thermal stress, while increasing the folding degree suppresses thermal stress across all graphene weight fractions, indicating that folding effectively reduces thermal stress generation in the material.

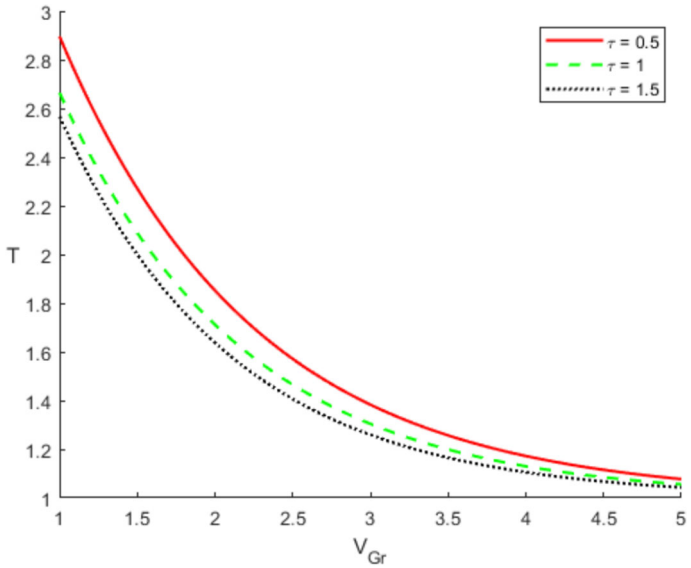


Fig. 15 Effect of thermal stress (T) as a function of volume fraction (V_{Gr}) under different (τ) values

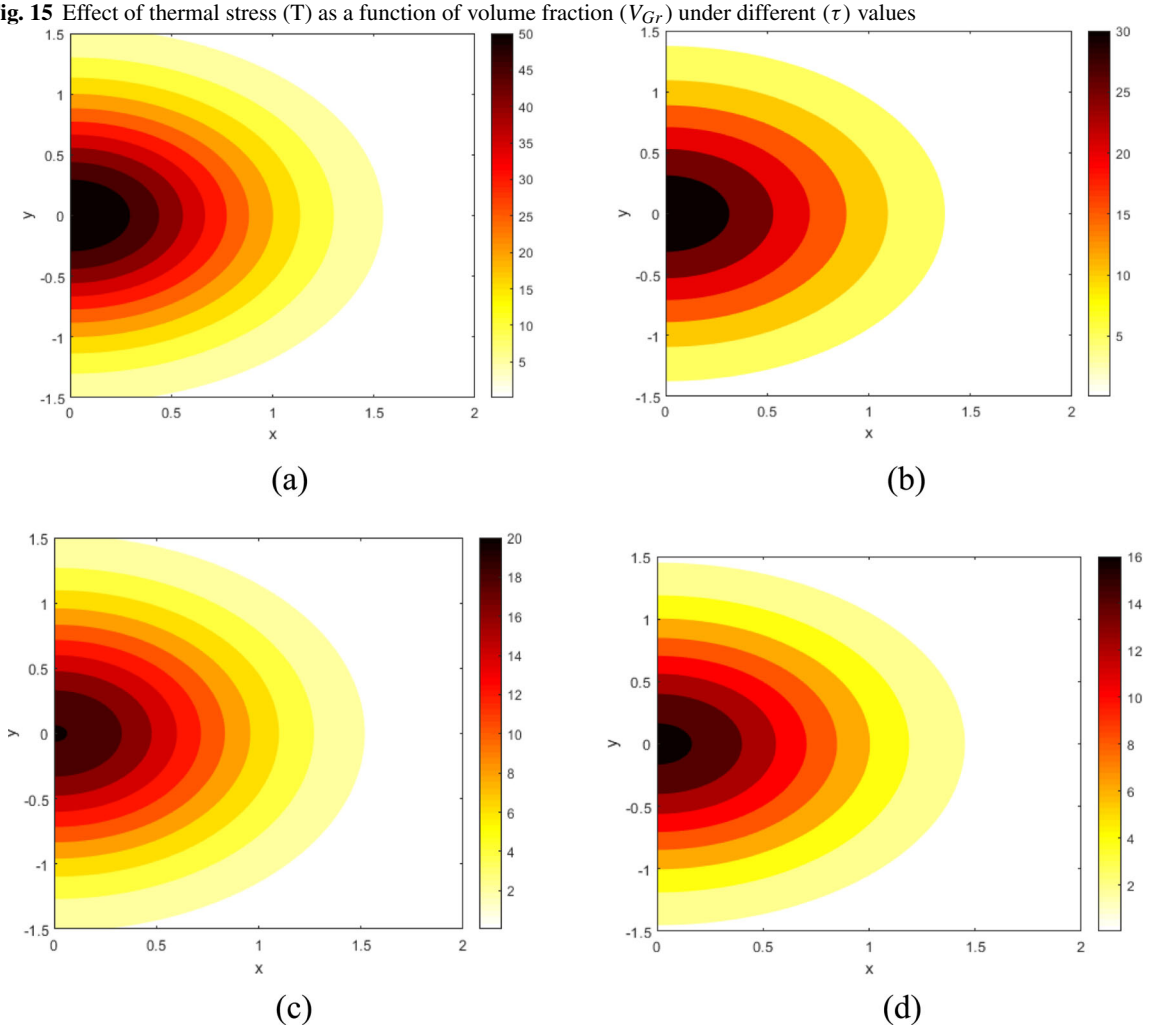


Fig. 16 Contour maps of thermal stress (T) for varying couple-stress parameters**a** l =0.2,**b** l =0.4,**c** l =0.6,**d** l =0.8

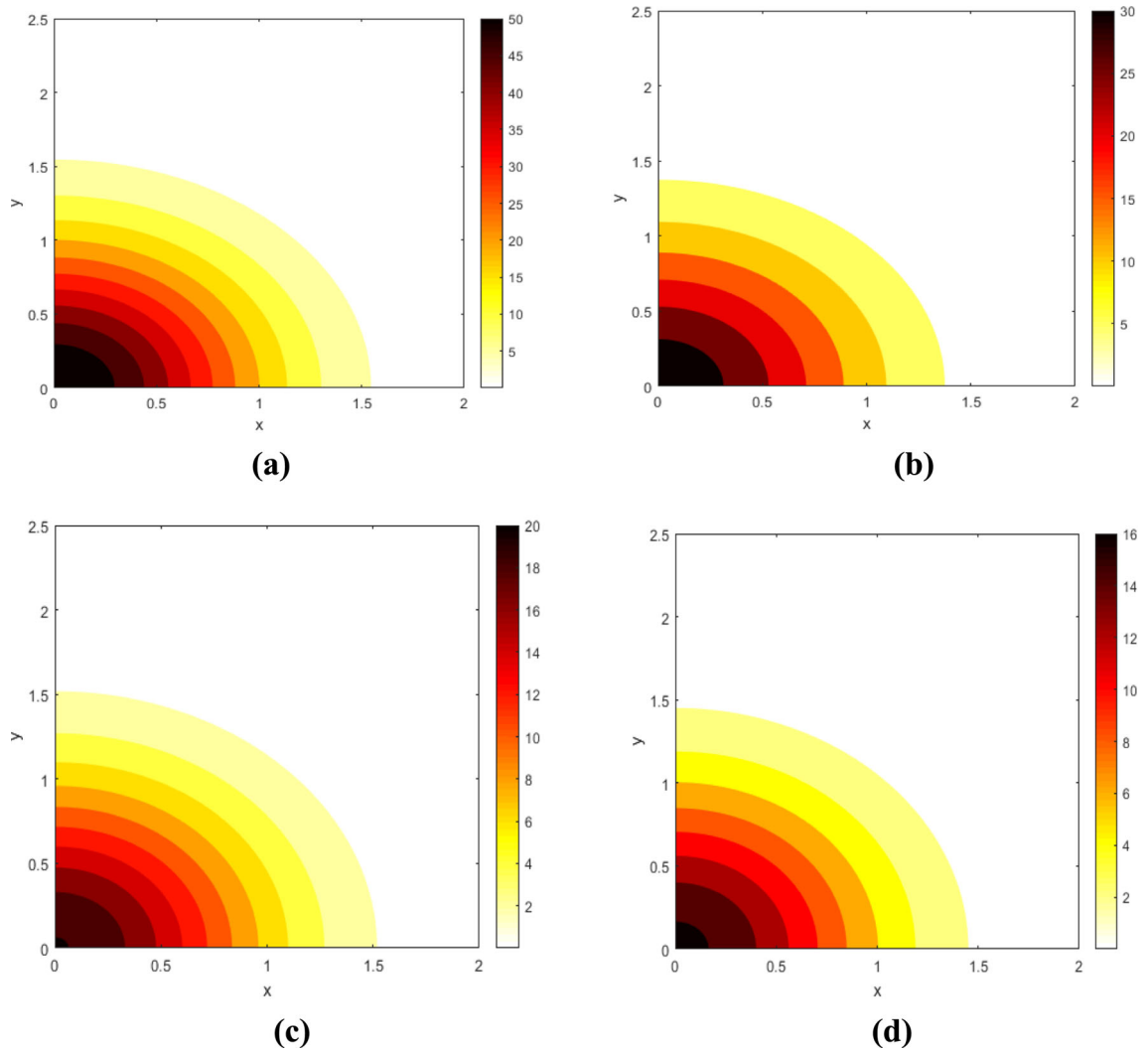


Fig. 17 Contour maps of thermal stress (T) for different DM theory parameters**a** $\eta = 0.25$,**b**$\eta = 0.5$,**c**$\eta = 0.75$,**d**$\eta = 1$

- Lower time-delay parameters produce higher normal stress and larger peak displacement, whereas increasing the time-delay parameter leads to an earlier and more pronounced reduction in these responses, thereby weakening the material's mechanical performance.
- Higher time-delay factors lead to a larger magnetic field and more pronounced Maxwell's stress response, while they also significantly reduce thermal stress, indicating their crucial role in influencing the dynamic behavior of the system.
- The contours confirm that thermal stress diminishes with increasing couple-stress and DM parameters, which are associated with reduced resonant frequencies.

Author contribution Rajendran Selvamani: Conceptualization, Investigation, Writing – original draft, Visualization, Supervision Thangamuni Prabhakaran: Data curation, Methodology, Project administration, Writing – original draft Murat Yaylacı: Writing – review & editing, Supervision, Project administration, Dursun Murat Sekban: Writing – review & editing, Visualization, Validation Ecren Uzun Yaylacı: Writing – review & editing, Resources, Software.

Funding Open access funding provided by the Scientific and Technological Research Council of Türkiye (TÜBİTAK). None.

Data availability The data that support the findings of this study are available on request from the authors.

Declarations

Conflict of interest The authors declare no competing interests.

Ethical approval The authors declare that the research was conducted according to ethical standards. This article does not contain any studies with human or animal subjects.

Consent to participate No external participants have contributed to the work discussed in this manuscript.

Consent for publication The authors give their full consent to the editor to publish this article if accepted.

Open Access This article is licensed under a Creative Commons Attribution 4.0 International License, which permits use, sharing, adaptation, distribution and reproduction in any medium or format, as long as you give appropriate credit to the original author(s) and the source, provide a link to the Creative Commons licence, and indicate if changes were made. The images or other third party material in this article are included in the article's Creative Commons licence, unless indicated otherwise in a credit line to the material. If material is not included in the article's Creative Commons licence and your intended use is not permitted by statutory regulation or exceeds the permitted use, you will need to obtain permission directly from the copyright holder. To view a copy of this licence, visit http://creativecommons.org/licenses/by/4.0/.

References

1. Eda, G., Fanchini, G., Chhowalla, M.: Large-area ultrathin films of reduced graphene oxide as a transparent and flexible electronic material. Nat. Nanotechnol. **3**(5), 270–274 (2008)
2. Li, D., Müller, M.B., Gilje, S., Kaner, R.B., Wallace, G.G.: Processable aqueous dispersions of graphene nanosheets. Nat. Nanotechnol. **3**(2), 101–105 (2008)
3. Potekin, R., Kim, S., McFarland, D.M., Bergman, L.A., Cho, H., Vakakis, A.F.: A micromechanical mass sensing method based on amplitude tracking within an ultra-wide broadband resonance. Nonlinear Dyn. **92**(2), 287–304 (2018)
4. Mahmoud, M.A.: Validity and accuracy of resonance shift prediction formulas for microcantilevers: a review and comparative study. Crit. Rev. Solid State Mater. Sci. **41**(5), 386–429 (2016)
5. Ji, Y., Choe, M., Cho, B., Song, S., Yoon, J., Ko, H.C., Lee, T.: Organic nonvolatile memory devices with charge trapping multilayer graphene film. Nanotechnology **23**(10), 105202 (2012)
6. Ramezani, S.R., Mojra, A.: Stability analysis of conveying-nanofluid CNT under magnetic field based on nonlocal couple stress theory and fluid-structure interaction. Mech. Based Des. Struct. Mach. **51**(1), 583–600 (2023)
7. Ouakad, H.M., Sedighi, H.M., Younis, M.I.: One-to-One and Three-to-One Internal Resonances in MEMS Shallow Arches. J. Comput. Nonlinear Dynam. **12**(5), 051025 (2017)
8. Moory-Shirbani, M., Sedighi, H.M., Ouakad, H.M., Najar, F.: Experimental and mathematical analysis of a piezoelectrically actuated multilayered imperfect microbeam subjected to applied electric potential. Compos. Struct. **184**, 950–960 (2018)
9. Abouelregal, A.E., Marin, M.: The size-dependent thermoelastic vibrations of nanobeams subjected to harmonic excitation and rectified sine wave heating. Mathematics **8**(7), 1128 (2020)
10. Eringen, A.C., Edelen, D.G.B.: On nonlocal elasticity. Int. J. Eng. Sci. **10**(3), 233–248 (1972)
11. Eringen, A.C.: On differential equations of nonlocal elasticity and solutions of screw dislocation and surface waves. J. Appl. Phys. **54**(9), 4703–4710 (1983)
12. Narendar, S., Gupta, S.S., Gopalakrishnan, S.: Wave propagation in single-walled carbon nanotube under longitudinal magnetic field using nonlocal Euler-Bernoulli beam theory. Appl. Math. Model. **36**(9), 4529–4538 (2012)
13. Salehipour, H., Shahidi, A.R., Nahvi, H.: Modified nonlocal elasticity theory for functionally graded materials. Int. J. Eng. Sci. **90**, 44–57 (2015)
14. Anh, N.D., Hieu, D.V.: Nonlinear random vibration of functionally graded nanobeams based on the nonlocal strain gradient theory. Acta Mech. **233**, 1633–1648 (2022)
15. Attia, M.A., Shanab, R.A.: On the dynamic response of bi-directional functionally graded nanobeams under moving harmonic load accounting for surface effect. Acta Mech. **233**, 3291–3317 (2022)
16. Boyina, K., Piska, R., Natarajan, S.: Nonlocal strain gradient model for thermal buckling analysis of functionally graded nanobeams. Acta Mech. **234**, 5053–5069 (2023)
17. Eroğlu, M., Esen, İ, Koç, M.A.: Thermal vibration and buckling analysis of magneto-electro-elastic functionally graded porous higher-order nanobeams using nonlocal strain gradient theory. Acta Mech. **235**, 1175–1211 (2024)
18. Selvamani, R., Thangamuni, P., Yaylacı, M., Emin Özdemir, M., Yaylacı, E.U.: Nonlinear vibration and parametric excitation of magneto-thermo elastic embedded nanobeam using homotopy perturbation technique. ZAMM-J. Appl. Math. Mech./Zeitschrift für Angewandte Mathematik und Mechanik **104**(12), e202400525 (2024)
19. Prabhakaran, T., Selvamani, R., Mahaveersreejayan, M., Wang, L.: Investigation of the effect of viscosity and density on the wave propagation of a nonlocal porous beam submerged in fluid using bernstein polynomials. Eng. Trans. **72**(3), 365–385 (2024)
20. Selvamani R., Prabhakaran T., Rubine L., Jayan M., Wang L.: Vibration of nonhomogeneous porous Euler nanobeams using Bernstein polynomials for boundary characteristics. Songklanakarin J. Sci. Technol. **46**(2) (2024)
21. Selvamani, R., Prabhakaran, T., Ebrahimi, F.: Damping characteristics of nonlocal strain gradient waves in thermoviscoelastic graphene sheets subjected to nonlinear substrate effects. Phys. Mesomech. **27**(4), 461–471 (2024)

22. Selvamani, R., Prabhakaran, T., Yaylacı, M., Kartal, ŞE., Yaylacı, E.U.: Doublet structural modeling of nonhomogeneous Euler mass sensor nanobeams using boundary characteristics Bernstein Polynomials. ZAMM-J. Appl. Math. Mech. / Zeitschrift für Angewandte Mathematik und Mechanik **105**(3), e202401264 (2025)
23. Selvamani, R., Rubine, L., Prabhakaran, T., Yaylaci, M.: Free vibration analysis of a functionally graded magneto-piezo-thermoelastic ceramic-metal nanobeam using modified nonlocal state-space strain gradient theory. Phys. Mesomech. **28**(2), 263–274 (2025)
24. Rajendran, S., Loganathan, R., Yaylaci, M., Yaylaci, E.U., Ozdemir, M.E.: Vibration of piezo-magneto-thermoelastic FG nanobeam submerged in fluid with variable nonlocal parameter. Adv. Nano Res. **16**(5), 489–500 (2024)
25. Selvamani, R., Ebrahimi, F., Yaylacı, M., Öztürk, Ş, Yaylacı, E.U.: Nonlinear poro-thermo-forced vibration in curved sandwich magneto-electro-elastic shells under hygrothermal environment. Acta Mech. **235**(9), 5489–5528 (2024)
26. Ghadiri, M., Rajabpour, A., Akbarshahi, A.: Non-linear forced vibration analysis of nanobeams subjected to moving concentrated load resting on a viscoelastic foundation considering thermal and surface effects. Appl. Math. Model. **50**, 676–694 (2017)
27. Adomian, G.: A review of the decomposition method in applied mathematics. J. Math. Anal. Appl. **135**, 501–544 (1988)
28. Lai, H.-Y., Hsu, J.-C., Kuo, C.-H.: An innovative eigenvalue problem solver for free vibration of Euler-Bernoulli beam by using the Adomian decomposition method. Comput. Math. Appl. **56**, 3204–3220 (2008)
29. Eltaher, M.A., Mahmoud, F.F., Assie, A.E., Meletis, E.I.: Coupling effects of nonlocal and surface energy on vibration analysis of nanobeams. Appl. Math. Comput. **224**, 760–774 (2013)
30. Reddy, J.N.: Nonlocal theories for bending, buckling and vibration of beams. Int. J. Eng. Sci. **45**(2), 288–307 (2007)
31. Hedrih, K.: The transversal creeping vibrations of a fractional derivative order constitutive relation of nonhomogeneous beam. Math. Probl. Eng. **2006**(1), 046236 (2006)
32. Atanackovic T.M., Pilipovic S., Stankovic B., Zorica D.: Fractional calculus with applications in mechanics: vibrations and diffusion processes. John Wiley & Sons (2014)
33. Caputo, M., Fabrizio, M.: A new definition of fractional derivative without singular kernel. Prog. Fract. Diff. Appl. **1**(2), 73–85 (2015)
34. Atangana A., Baleanu D.: New fractional derivatives with nonlocal and non-singular kernel: theory and application to heat transfer model. http://arxiv.org/abs/1602.03408 (2016)
35. Ezzat, M.A., El Karamany, A.S., Fayik, M.A.: Fractional order theory in thermoelastic solid with three-phase lag heat transfer. Arch. Appl. Mech. **82**(4), 557–572 (2012)
36. Qi, Z., Peng, W., He, T.: Investigation on the thermoelastic response of a nanobeam in modified couple stress theory considering size-dependent and memory-dependent effects. J. Therm. Stresses **45**(10), 773–792 (2022)
37. Abouelregal, A.E., Dargail, H.E.: Memory and dynamic response of a thermoelastic functionally graded nanobeams due to a periodic heat flux. Mech. Based Des. Struct. Mach. **51**(4), 2154–2176 (2023)
38. Li, Y., Zhang, P., Li, C., He, T.: Fractional order and memory-dependent analysis to the dynamic response of a bi-layered structure due to laser pulse heating. Int. J. Heat Mass Transf. **144**, 118664 (2019)
39. Yu, Y.-J., Hu, W., Tian, X.-G.: A novel generalized thermoelasticity model based on memory-dependent derivative. Int. J. Eng. Sci. **81**, 123–134 (2014)
40. Gul, U., Aydogdu, M., Gaygusuzoglu, G.: Axial dynamics of a nanorod embedded in an elastic medium using doublet mechanics. Compos. Struct. **160**, 1268–1278 (2017)
41. Gul, U., Aydogdu, M.: Hygro-thermal vibration behavior of porous functionally graded nanobeams based on doublet mechanics. Arch. Mech. **76**(5), 413 (2024)
42. Gul, U., Aydogdu, M.: Structural modelling of nanorods and nanobeams using doublet mechanics theory. Int. J. Mech. Mater. Des. **14**(2), 195–212 (2018)
43. Granik, V.T., Ferrari, M.: Microstructural mechanics of granular media. Mech. Mater. **15**(4), 301–322 (1993)
44. Ebrahimian, M.R., Imam, A., Najafi, M.: Doublet mechanical analysis of bending of Euler-Bernoulli and Timoshenko nanobeams. ZAMM-J. Appl. Math. Mech. / Zeitschrift für Angewandte Mathematik und Mechanik **98**(9), 1642–1665 (2018)
45. Ebrahimi, F., Ahari, M.F.: On the buckling of meta-graphene-origami-enabled magnetostrictive nanoplates under temperature gradient. Acta Mech. **235**(5), 2611–2628 (2024)
46. Karami, B., Ghayesh, M.H.: Forced vibration behaviour of elastically constrained graphene origami-enabled auxetic metamaterial beams. Math. Comput. Appl. **30**(1), 5 (2025)
47. Zhu, Y., Charkieh, A.S., Polyzos, E., Pyl, L.: Tunable flexural properties of sandwich structures with Miura and creaseless herringbone buckling pattern cores via geometrical modifications. Compos. Struct. **371**, 119463 (2025)
48. Garg, A., Zheng, W., Avcar, M., Belarbi, M.-O., Kiran, R., Li, L., Raman, R.: Free vibration behaviour of curved Miura-folded bio-inspired helicoidal laminated composite cylindrical shells using HSDT assisted by machine learning-based IGA. Compos. Struct. **357**, 118933 (2025)
49. Lucarini, S., Hossain, M., Garcia-Gonzalez, D.: Recent advances in hard-magnetic soft composites: Synthesis, characterisation, computational modelling, and applications. Compos. Struct. **279**, 114800 (2022)
50. Selvamani, R., Prabhakaran, T., Yaylacı, M., Öztürk, Ş, Uzun Yaylacı, E.: Fractional nonlocal couple stress waves in magnetoelastic nanobeam using homotopy perturbation technique. Acta Mech. (2025). https://doi.org/10.1007/s00707-025-04431-5
51. Ghannadpour, S., Mohammadi, B., Fazilati, J.: Bending, buckling and vibration problems of nonlocal Euler beams using Ritz method. Compos. Struct. **96**, 584–589 (2013). https://doi.org/10.1016/j.compstruct.2012.08.024
52. Phadikar, J., Pradhan, S.: Variational formulation and finite element analysis for nonlocal elastic nanobeams and nanoplates. Comput. Mater. Sci. **49**(3), 492–499 (2010). https://doi.org/10.1155/2020/8786373

Publisher's Note Springer Nature remains neutral with regard to jurisdictional claims in published maps and institutional affiliations.